PCCP

# Nonmonotonic Thickness-dependence of In-plane Thermal Conductivity of Few-Layered $MoS_2$: 2.4 to 37.8 nm


| | |
|---|---|
| Journal: | *Physical Chemistry Chemical Physics* |
| Manuscript ID | CP-ART-05-2018-002858.R2 |
| Article Type: | Paper |
| Date Submitted by the Author: | 11-Sep-2018 |



| | |
|---|---|
| Complete List of Authors: | Yuan, Pengyu; Iowa State University, Mechanical engineering<br>Wang, Ridong; Iowa State University, Mechanical Engr.<br>Wang, Tianyu; Iowa State University<br>Wang, Xinwei; Iowa State University, Mechanical Engr.<br>Xie, Yangsu; Shenzhen University |

# Nonmonotonic Thickness-dependence of In-plane Thermal Conductivity of Few-Layered $MoS_2$: 2.4 to 37.8 nm

Pengyu Yuan[1,§], Ridong Wang[1,§], Tianyu Wang[1], Xinwei Wang[1,*], Yangsu Xie[2,*]

[1]Department of Mechanical Engineering, Iowa State University, Ames, IA 50011, USA

[2]College of Chemistry and Environmental Engineering, Shenzhen University, Shenzhen, Guangdong, 518055, P. R. China

[§] These authors contributed equally to this work.

* Correspondence:

Xinwei Wang: xwang3@iastate.edu, +1-515-294-8023 (phone);

Yangsu Xie: ysxie@szu.edu.cn, +86-755-26922241 (phone).

Email Address:

Pengyu Yuan: pyuan@iastate.edu

Ridong Wang: rdwang@iastate.edu

Tianyu Wang: tywang@iastate.edu

**Abstract**

Recent first-principles modeling reported a decrease of in-plane thermal conductivity ($k$) with increased thickness for few layered $MoS_2$, which is resulted from the change in phonon dispersion and missing symmetry in the anharmonic atomic force constant. For other 2D materials, it has been well documented that a thicker one could have a higher in-plane $k$ due to their lower density of surface disorders. However, the effect of thickness on the $k$ of $MoS_2$ has not been systematically uncovered by experiments. In addition, from either experimental or theoretical approaches, in-plane $k$ of tens-nm-thick $MoS_2$ is still missing, which makes the physics on the thickness-dependent $k$ remain ambiguous. In this work, we measure the $k$ of few-layered (FL) $MoS_2$ with thickness spanning a large range: 2.4 nm to 37.8 nm. A novel five energy transport state-resolved Raman (ET-Raman) method is developed for the measurement. For the first time, the critical effect of hot carrier diffusion, electron-hole recombination, and energy coupling with phonons are taken into consideration when determining $k$ of FL $MoS_2$. By eliminating the use of laser energy absorption data and Raman temperature calibration, unprecedented data confidence is achieved. A nonmonotonic thickness-dependent $k$ trend is discovered. $k$ decreases from 60.3 W/m·K (2.4 nm thick) to 31.0 W/m·K (9.2 nm thick), and then increases to 76.2 W/m·K (37.8 nm thick), which is close to the reported $k$ of bulk $MoS_2$. This nonmonotonic behavior is analyzed in detail and attributed to the change of phonon dispersion for very thin $MoS_2$ and reduced surface scattering effect for thicker samples.

**Keywords**: thermal conductivity, thickness dependence, picosecond laser heating, hot carrier diffusion, interface phonon transport, Raman spectroscopy

## 1. Introduction

Since the discovery of graphene in 2004,[1] extensive research has been conducted on two-dimensional (2D) materials,[2, 3] such as hexagonal boron nitride,[4] transition metal dichalcogenides (TMDs),[5] and transition metal oxides,[6] due to their unique physical properties and potential technological applications in novel nanoelectronics, photonics, and many other fields. Compared with graphene, molybdenum disulfide ($MoS_2$) as one of TMDs, has shown similar or even superior properties due to its sizable bandgap changing from direct for single layer to indirect bandgap for few-layer as a result of quantum confinement [7] along with a decent electron mobility and high current on/off ratio.[8] The smaller size of 2D $MoS_2$ based devices makes it promising to be more efficient than conventional silicon-based electronics.[9-11] However, to realize the reliability and desired performance of 2D $MoS_2$ in novel electronics requires sophisticated understanding and control of thermal transport at the nanoscale.[12, 13] A high thermal conductivity ($k$) will facilitate fast heat dissipation during device operation, while a low $k$ can enhance the thermoelectric conversion efficiency in thermoelectric devices.[14] Additionally, different from conventional thin films (e.g. silicon thin film), the weak van der Waals interaction between layers of 2D $MoS_2$ makes the strength of boundary scattering much weaker for in-plane phonon transport.[15] This will lead to a quite different thickness dependent trend for $k$. Thus, fast and accurate $k$ measurement of 2D $MoS_2$, especially the thickness dependent $k$ is significant for understanding the thermal performance and energy transport of 2D $MoS_2$ from both the fundamental and applied points of view.[15-18]

Over the past decades, significant progress has been made in the $k$ study of 2D $MoS_2$ by both experiment and theoretical simulation. In experimental works on few-layered (FL) $MoS_2$, the $k$

results are ranging from 15 W/m·K to 100 W/m·K.[12, 18-21] Just for single layered $MoS_2$, 34.5 W/m·K (ref. 17) and 84 W/m·K (ref. 22) have been reported. Since both sample quality and experiment conditions are different, direct comparison among those results will be less convincing. For theoretical methods, molecular dynamics (MD) simulation using Stillinger-Weber potential gives a thickness-independent *k* of 19.76 W/m·K for FL $MoS_2$. [16] One recent first-principles-driven approach [23] is applied to study *k* of one- to three-layered $MoS_2$ which agrees with most experimental results. Other works discovered that thicker 2D materials could have a higher in-plane *k* due to their lower density of surface disorders.[24] To solve this debate requires a systematic study of the *k*-thickness relationship of 2D $MoS_2$ through experiment. In addition, from either experimental or theoretical approaches, in-plane *k* of tens-nm-thick $MoS_2$ is still missing, which makes the systematic data on the thickness-dependent *k* remain ambiguous. Aside from the challenges and differences of different methods mentioned above, the effects from roughness,[25] lateral sizes,[26] and defects[27] can also make the measured *k* of 2D $MoS_2$ vary largely from different groups which leaves the intrinsic thermal properties uncovered. Therefore, for the thickness-dependent *k*, it is highly desirable to measure $MoS_2$ of different thickness with one single state-of-the-art technique.

Some well-known experimental techniques used for measuring *k* of 2D materials include the 3$\omega$ method,[28] the pump-probe thermoreflectance technique,[29] and the confocal micro-Raman technique.[30, 31] However, the results contain large experimental errors due to the following several mechanisms. In the 3$\omega$ method and pump-probe technique, the sample post-processing (e.g., metallic layer deposition and metal lines on samples' surface) could induce undesirable, yet unknown change in the intrinsic *k* of 2D materials. Thus, the non-invasive optothermal Raman

technique is more favored. To date, the non-contact and non-invasive optothermal Raman technique appears to be one of the most widely used techniques for studying thermal properties of 2D materials.[17, 22, 31, 32] However, there are still many challenges and possible origins of the measurement errors which limit its application.[33] First, in the confocal micro-Raman technique, one of the main factors determining the accuracy of the measured *k* is the laser absorption which is related to the interaction between the to-be-measured material and the incident light and the optical properties vary a lot from sample to sample.[17, 18] Thus, the reported scattered *k*- thickness profiles could partially come from the variation of laser absorption evaluation.[15] In addition, the values of the interfacial thermal resistance between the 2D $MoS_2$ and its substrate (*R*) also contribute to the *k* experiment errors. Even though *R* could be very small in most of the time, accurately determine and consider the interface thermal resistance is important for the *k* study of 2D $MoS_2$. Simply referring an *R* value from other independent experiments or even neglecting the effects of *R* could introduce large and yet unevaluated errors in the measured *k* value. Furthermore, for 2D semiconductor materials just like $MoS_2$, the optically generated hot carriers can strongly contribute to the thermal diffusion and heat dissipation during the micro-Raman measurement. [34] Yet in the previous work, the effect of hot carrier diffusion on thermal transport has not been fully taken into consideration. As a result, the real heating area is underestimated since the hot carrier diffusion could greatly extend the heating size. Therefore, laser heating flux is overestimated, which leads to less accurate *k* evaluation. Besides, the temperature coefficient calibration of the targeted 2D materials in the confocal micro-Raman technique also gives very large errors and increases the *k* uncertainty.[18, 35] Considering the possible error sources mentioned above, the measurement uncertainty of *k* by the confocal micro-Raman technique could reach as large as ±40%.[36]

Herein, we systematically measure the in-plane $k$ and study the effect of thickness of FL $MoS_2$ supported on a glass substrate. To this end, a five-state energy transport state-resolved Raman (ET-Raman) approach with energy transport states variations at both space and time domains is developed. By using this technique, the effect of interface thermal resistance and hot carrier diffusion is carefully taken into consideration in the $k$ measurement, which significantly improves the measurement accuracy. In addition, the interface thermal resistance and hot carrier diffusivity are quantitatively and simultaneously determined. The large measurement errors introduced by laser absorption evaluation and Raman properties' temperature coefficient calibration are completely eliminated. The result of this work gives a far more accurate understanding of the intrinsic thermal properties of 2D $MoS_2$ materials.

## 2. Experimental methods

### 2.1 Sample preparation and characterization

In this work, eight FL supported $MoS_2$ samples are prepared by micromechanical cleavage technique. The bulk $MoS_2$ crystal (429MS-AB, molybdenum disulfide, small crystals from the U.S.A., SPI Suppliers) is first peeled off using adhesive Scotch tape and Gel film. These freshly cleaved thin crystals on Gel film are then transferred to a clean glass substrate and rubbed with a cotton swab to increase the contact. After the Gel film is removed, FL $MoS_2$ nanosheets are left on the substrate. Here, instead of preparing suspended structure, we use a substrate to support the sample to study its thermal properties. The reason is that in most applications, 2D materials are integrated into devices and supported on substrates.[37] The lateral size of layered $MoS_2$ nanosheets has an equivalent radius ranging from 7.5 to 13 μm. The thickness of different

samples was measured using atomic force microscopy (AFM), as shown in Figure 1. The height profiles are presented as the red dashed lines in the AFM images. The samples have a thickness of 2.4, 3.6, 5.0, 9.2, 15.0, 24.6, 30.6 and 37.8 nm, respectively. The blue dashed square in each sample AFM image shows the area where the laser is focused during Five-State ET-Raman experiments. We also evaluate the sample surface roughness along the center yellow line in the blue dashed square, from which the root-mean-square (RMS) roughness ($R_q$) of the samples are calculated and shown in the figures. $R_q$ varies a little bit for different samples. For example, $R_q$ is 0.46 nm and 0.57 nm for the 2.4 nm-thick sample and the 24.6 nm-thick samples respectively. For comparison, the substrate (glass) surface has an $R_q$ (glass) around 1.6 nm.

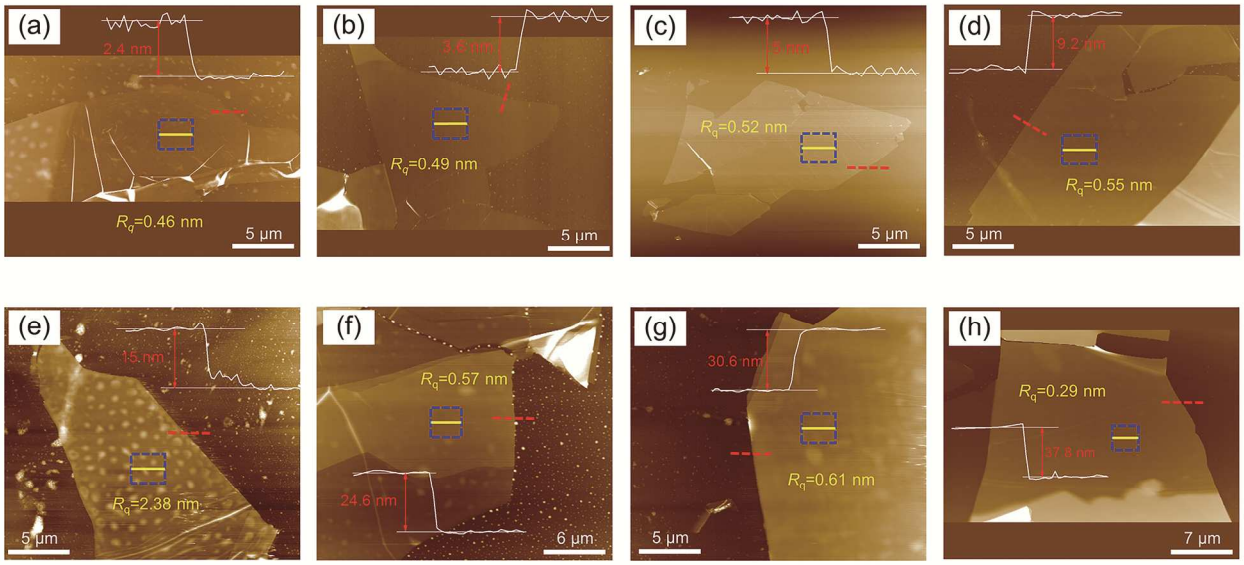


**Figure 1.** (a)-(g) AFM images of 2.4, 3.6, 5.0, 9.2, 15.0, 24.6, 30.6 and 37.8 nm thick $MoS_2$ on glass substrate. The blue dashed box indicates the area where the Raman experiment is performed. The yellow center line corresponds to where the RMS roughness $R_q$ value is obtained. The height profiles are measured along the red dashed lines in the AFM images.

### 2.2 Energy transport state-resolved Raman for *k* characterization

#### A. Variation of laser spot size to differentiate the effect of *k*, *D*, and *R* in steady state

In this work, Raman spectroscopy is used to measure the thermal conductivity of $MoS_2$ samples by probing the variation of the Raman shift under simultaneous laser heating. As shown in Fig. 2a, under laser heating, three physical processes take place, which all affect the thermal response of the sample. The first one is the hot carrier generation, diffusion in space, and electron-hole recombination. This process introduces heat transfer and energy redistribution, and the process is determined by the hot carrier diffusivity ($D$). The subsequent second process is the heat conduction by phonons, which receives energy from the hot carriers or electron-hole recombination. Such heat conduction hinges on the thermal conductivity ($k$) of the sample, mainly the in-plane thermal conductivity. The third process is the heat conduction from the $MoS_2$ sample to the substrate, and this process is dominated by the local thermal resistance ($R$).[34] Under steady state, the governing equation for the hot carrier transport is:[38, 39]

$$\Phi\alpha + D\frac{1}{r}\frac{\partial}{\partial r}\left(r\frac{\partial \Delta N}{\partial r}\right) - \frac{\Delta N}{\tau} + \frac{\partial n_0}{\partial T_{\mathrm{CW}}}\frac{\Delta T_{\mathrm{CW}}}{\tau} = 0, \quad (1)$$

where $D$ ($m^2/s$), $\tau$ (s), and $\Delta T_{\mathrm{CW}}(r,t)$ (K), are the hot carrier diffusivity, carrier lifetime, and temperature rise. $\Phi$ (photon counts/$m^3 \cdot s$) is the incident photon flux and $\alpha$ is the laser absorptivity. $\Phi\alpha$ is the hot carrier photo-generation source. $n_0$ ($m^{-3}$) is the equilibrium free-carrier density at temperature $T$. The second term on the left side describes the hot carrier diffusion. The third term ($\Delta N/\tau$) represents the electron-hole recombination which will decrease the carrier density. The last term $(\partial n_0 / \partial T_{\mathrm{CW}})\Delta T_{\mathrm{CW}} / \tau$ is for thermal activation which gives the carrier generation due to temperature rise, which is negligible in our work because of the relatively low temperature rise and free-carrier density.[34, 38] More details of this treatment can be found in

Supplementary Information section S1.

For the thermal transport sustained by phonons, the governing equation can be written as:

$$(h\nu - E_g)\Phi\alpha + E_g\Delta N/\tau + k_{\square}\frac{1}{r}\frac{\partial}{\partial r}(r\frac{\partial \Delta T_{\mathrm{CW}}}{\partial r}) + k_{\perp}\frac{\partial^2 \Delta T_{\mathrm{CW}}}{\partial z^2} = 0, \quad (2)$$

where $E_g$ (J) is $MoS_2$ bandgap. $k_{\square}$ and $k_{\perp}$ are the in-plane and cross-plane thermal conductivity of FL $MoS_2$. This anisotropy is immanent in most 2D materials: along the in-plane direction, atomic bonds are largely covalent; while along the out-of-plane direction, atomic interaction is dominated by the weak van der Waals force. In this equation, $h\nu$ (2.33 eV) is the photon energy of the laser beam. $(h\nu - E_g)\Phi\alpha$ describes the heat generation from the fast thermalization process. $E_g\Delta N/\tau$ is related to the energy coupling to phonons from the electron-hole recombination. Due to the large ratio between sample's lateral size (8–13 μm) and thickness (< 40 nm), we only consider the in-plane direction hot carrier diffusion. For the heat transfer across the $MoS_2$/glass structure, the interface heat flux can be expressed as: $q'' = (T_{\mathrm{MoS_2}} - T_{\mathrm{Si}})/R$ ($q''$: interface heat flux, $T_{\mathrm{MoS_2}}$ and $T_{\mathrm{Si}}$ are the temperature of $MoS_2$ and glass substrate immediately next to the interface).

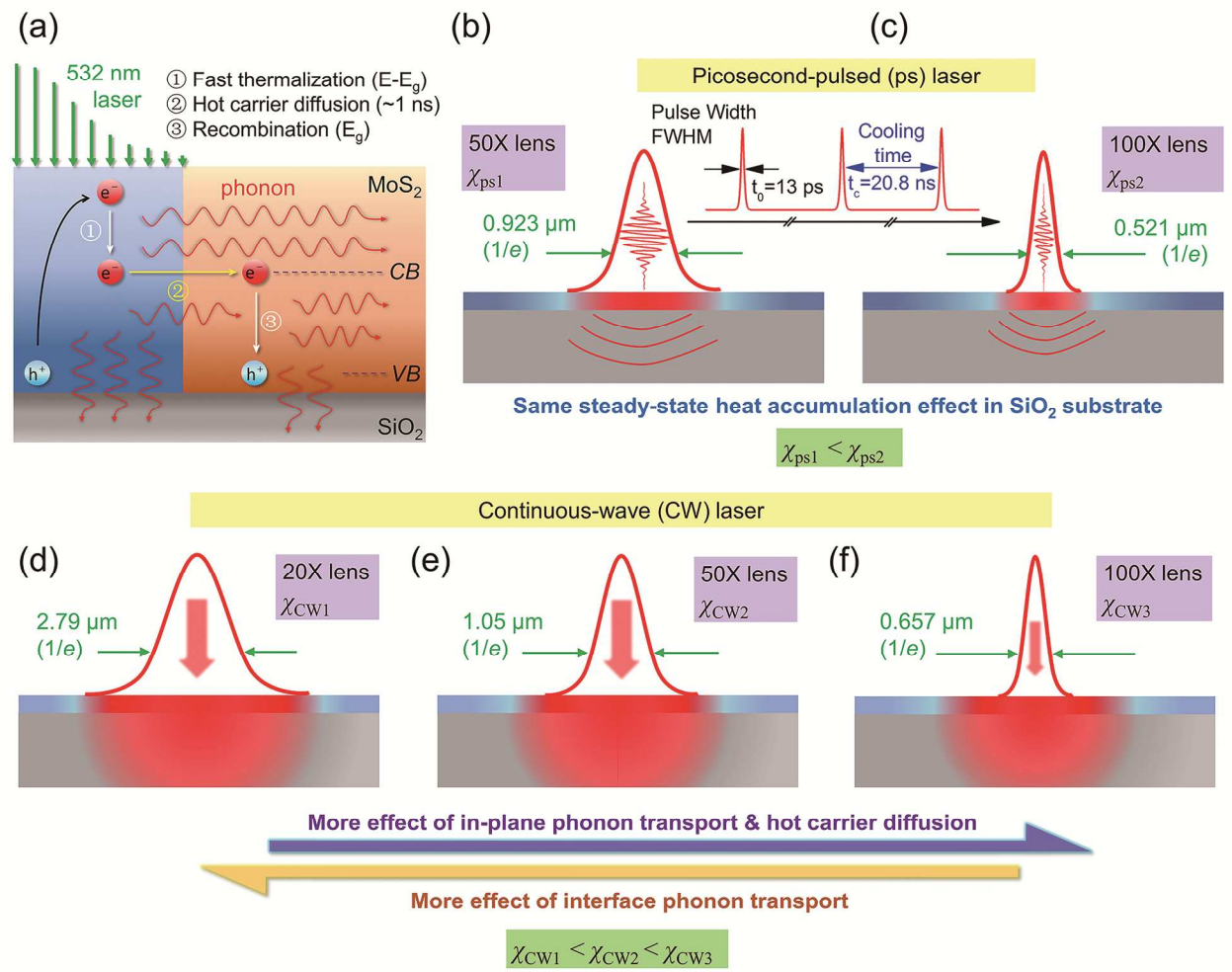


**Figure 2.** The schematic for the physical principle of Five-State Picosecond ET-Raman. (a) The generation, diffusion, and recombination of the hot carrier in $MoS_2$ upon laser illumination (not to scale). (b)(c) Two sub-states in ps laser (pulse width FWHM is 13 ps, pulse period is 20.8 ns) heating under 50× and 100× objectives. (b)-(f) Three sub-states in CW laser heating under 20×, 50×, and 100× objectives to achieve different laser spot size heating to differentiate the effects of *R*, *k*, and *D*.

To measure the in-plane thermal conductivity of $MoS_2$, all the interface energy transport and hot carrier effect must be considered. The effect of *k*, *D*, and *R* on heat transfer indeed varies with the laser heating spot size. This, in concept and analogy, can be explained by the circular fin heat

transfer $q = 2\pi k r_0 t \Delta T m \frac{K_1(mr_0)I_1(mr_1) - I_1(mr_0)K_1(mr_1)}{K_0(mr_0)I_1(mr_1) + I_0(mr_0)K_1(mr_1)}$, where $k$, $t$, and $r_1$ is the in-plane thermal conductivity, the thickness, and lateral size (radius) of 2D material, $r_0$ is the radius of laser heating spot, $m=(k \cdot t \cdot R)^{-1}$. The hot carrier's effect is strongly related to the diffusion in space, and the heat transfer by hot carriers can be approximated as $q_e = (\partial N / \partial r) 2\pi r_0 D t E_g$. Thus, the thermal energy transport by phonons and hot carriers follow different rules as a function of laser heat spot size. Based on this, the effect of $D$, $k$, $R$ can be differentiated by designing steady state heating with different laser heating sizes.

In our ET-Raman technique, three steady-state heating with different laser spot sizes are designed. Experimental setup could be found in Supplementary Information Figure S1. As shown in Fig. 2 (d) - (f), by using different objectives (20×, 50×, and 100×) to have the size variation, the effect of $R$, $D$, and $k$ will be differentiated. Under CW laser heating, by varying laser powers ($P$), a parameter called Raman shift power coefficient (RSC) can be obtained: $\chi_{CW}=\partial\omega/\partial P$. $\chi_{CW}$ is determined by $R$, $D$, and $k$, laser absorption coefficient, and temperature coefficient of Raman shift. For the three heating states shown in Fig. 2(d)-(f), we have $\chi_{CW3} > \chi_{CW2} > \chi_{CW1}$ considering the larger energy density under a more tightly focused laser beam. When the heating spot size decreases, the effect of $D$ and $k$ of the 2D material on the measured temperature becomes more significant, while the effect of $R$ is reduced. In an extreme case, when the laser heating spot size is larger than 2D material, the measured temperature rise will be dominated by the interface thermal resistance ($R$). Therefore, through these three steady-state constructions, the effect of $k$, $D$, and $R$ in the measured RSC can be differentiated.

**B. Pico-second Raman to introduce strong $\rho c_p$ effect**

To determine the thermal conductivity *k*, past Raman techniques require the laser absorption data. In addition, temperature coefficient pre-calibration of the Raman properties to determine the real temperature rise of the sample during laser heating is necessary. These two factors bring in large uncertainties in the resulting *k*. In our ET-Raman, we avoid the two factors by designing two picosecond-pulsed laser heating states (laser wavelength: 532 nm, pulse duration: 13 ps, repetition rate: 48.2 MHz) in Raman experiment. In the two ps laser heating states, near zero-transport can be assumed and the effect of $\rho c_p$ ($\rho$: density, $c_p$: specific heat) is dominating. During the ps laser heating, phonon transport has very limited contribution to thermal energy dissipation. Considering that hot electrons and holes cool quickly (~0.6 ps) by transferring energy to phonons,[40] we can use single temperature to evaluate this fast thermalization process. More information about ps laser heating is included in Supplementary Information section S1. By only considering the laser absorption in $MoS_2$ sample, the energy balance equation can be expressed as:

$$\rho c_p \frac{\partial \Delta T_{\mathrm{ps}}}{\partial t} = k_{\square} \frac{1}{r} \frac{\partial}{\partial r} \left( r \frac{\partial \Delta T_{\mathrm{ps}}}{\partial r} \right) + k_{\perp} \frac{\partial^2 \Delta T_{\mathrm{ps}}}{\partial z^2} + \alpha Q \left( \frac{hv - E_g}{hv} \right), \tag{3}$$

where $Q$ (W/m$^3$) is the laser intensity, $t$ (s) is time, and $\Delta T_{\mathrm{ps}}(\mathrm{r},t)$ represents the temperature rise in the zero-transport state. The laser intensity (heat flux) is given by:

$$Q(r,z,t) = \frac{Q_0}{\tau_L} \exp\left(-\frac{r^2}{r_0^2}\right) \exp\left[ -\frac{\ln(2) t^2}{t_0^2} \right] \exp\left(-\frac{z}{\tau_L}\right), \tag{4}$$

where $Q_0$ (W/m$^3$) is the peak laser intensity, $r_0$ (m) is the laser spot radius, $t_0$ (6.5 ps) is half pulse width. $\tau_{\mathrm{L}} = \lambda / 4\pi k_{\mathrm{L}} = 38.5$ nm is the laser absorption depth of $MoS_2$. λ=532 nm is the laser wavelength, and $k_{\mathrm{L}}$ is the extinction coefficient.

In ps laser heating, within each pulse (13 ps), the thermal diffusion length for both $MoS_2$ and the glass substrate are much smaller than the laser spot size. Hence, the heat conduction in the laser heating region has an insignificant effect on the temperature rise. On the other hand, a steady-state heat accumulation effect should not be neglected since the relaxation time (20.8 ns) of the $MoS_2$ nanosheets supported on glass substrate is longer than the ps laser pulse interval.[41] Thus, two sub-states [Fig. 2 (b) and (c)] are generated under 50× (NA=0.5, 0.923 μm) and 100× (NA=0.8, 0.521 μm) objectives. In the similar way, we obtain RSC under both 50× and 100× objectives as $\chi_{ps1}$ and $\chi_{ps2}$, respectively. The heat accumulation effect can be eliminated by using the temperature difference under 50× and 100× objectives as $\Delta T_{ps}(100\times) - \Delta T_{ps}(50\times)$. More information about this treatment can be found in the Supplementary Information section S1.

Based on the measured RSC from the five heating states, three dimensionless normalized RSC can be obtained as $\Theta_1 = \chi_{CW1}/(\chi_{ps2}-\chi_{ps1})$, $\Theta_2 = \chi_{CW2}/(\chi_{ps2}-\chi_{ps1})$, and $\Theta_3 = \chi_{CW3}/(\chi_{ps2}-\chi_{ps1})$. With these normalized RSC, the effects of laser absorption, Raman temperature coefficients, and the pulse accumulation are completely ruled out. $\Theta$ is only a function of the 2D material and the substrate's $\rho c_p$, $R$, $k$, and $D$. Trial values of $R$, $D$, and $k$ combinations can be used to solve Eqs (1)-(3) to determine the theoretical $\Theta$. The trail value combination which gives $\Theta_i$ that matches the experimental data will be the real properties of the sample. It should be noted that the above governing equations take both $MoS_2$ and glass into consideration. All these are considered in our 3D modeling.

## 3. Results and Discussion

### 3.1 Thermal response of $MoS_2$ under CW and picosecond-pulsed laser heating

In the Raman experiments, as shown in Figure 3 (a)-(e), the laser heating size is determined by the spatial energy distribution for each heating state. Taking 20× objective with CW laser for example, as shown in Fig. 3 (a-1), the false color map data is obtained from the image captured by a CCD (charge-coupled-device) camera. The corresponding laser spot size (at $e^{-1}$) is determined to be 1.40 μm. Taking the 2.4-nm-thick $MoS_2$ sample for example, a typical Raman spectrum of $MoS_2$ under different heating states is shown in the first sub-figure (e.g., Fig. 3(a-1)). To extract the Raman frequency as a function of laser power, the Raman spectrum is fitted with the Lorenz function. To find the laser power coefficient (RSC), eight room-temperature Raman spectra are automatically collected at different laser power levels. In the specified laser power range for both CW and ps laser, the Raman shift linearly depends on the laser power, which can be expressed as: $\Delta\omega = \omega(P_2) - \omega(P_1) = \chi(P_2 - P_1) = \chi\Delta P$ . $\chi$ ($cm^{-1}$/mW) is the first-order Raman shift power coefficient (RSC) for $MoS_2$, and $P$ (mW) is the laser power (laser energy just before entering the sample surface). Here, we choose the Raman results from the $E^1_{2g}$ vibration mode to deduce RSC. The reason is that the interlayer interactions and the substrate have less effect on $E^1_{2g}$ mode.[42]

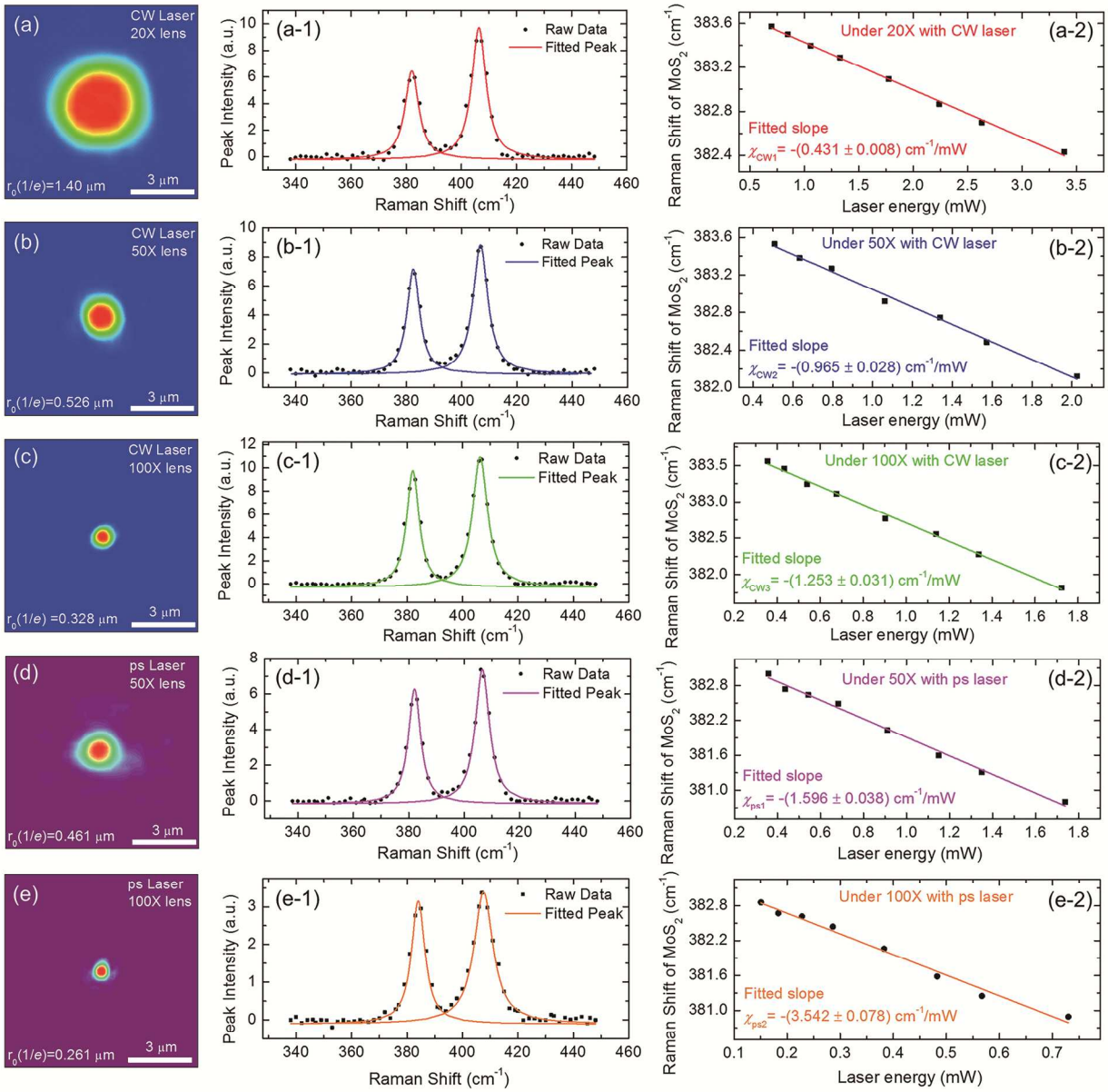


**Figure 3.** Spatial energy distribution of focused laser for the five heating states. The typical Raman spectrum and the linear fitting result (RSC) of 2.4 nm thick $MoS_2$ nanosheets at different heating states. The solid curves and lines are the fitted results.

By using a CW laser, the RSC of $MoS_2$ $E^1_{2g}$ mode is –(0.431±0.008) $cm^{-1}$/mW under 20× objective, –(0.965±0.028) $cm^{-1}$/mW under 50× objective, and –(1.253±0.031) $cm^{-1}$/mW under 100× objective. As shown in Fig. 3(a-2), (b-2) and (c-2), RSC increases with reduced heating

size due to the larger laser energy density. For ps laser heating scenarios, the laser power is maintained as low as possible to avoid photon absorption saturation and stay within the linear temperature dependence range for Raman properties. [41, 43-45] The linear dependence on the laser power for the three different heating sizes shows a very small standard error. This indicates that in the specified laser power range, there are no significant changes in the thermal properties of materials. For ps laser heating under 50× and 100× objectives, as shown in Fig. 3(d-2) and (e-2), the RSC values are –(1.596±0.038) $cm^{-1}$/mW and –(3.542±0.078) $cm^{-1}$/mW, respectively. Based on the RSC values from the five heating states, the normalized RSC is obtained as $\Theta_{exp\_1}$ = 0.222±0.011, $\Theta_{exp\_2}$ = 0.496±0.024, and $\Theta_{exp\_3}$ = 0.644±0.033. For the other seven samples, the RSC values are summarized in Table S1 in the Supplementary Information. Here, the uncertainty in RSC is only from a single linear fit. For each RSC value, we actually have measured several times, the one used in data processing is with the smallest uncertainty which is believed to reflect true property. It should be noted that the thickness dependent bandgap of $MoS_2$ is also considered in this work and summarized in Table S1. Additionally, for semiconductors, the band gap generally decreases with increased temperature. For instance, the bandgap of $MoSe_2$ changes with temperature as 0.0008 eV/K.[46] In our experiment, the highest temperature rise is only around 75 K, which gives negligible change in the bandgap.

### 3.2 Simultaneous determination of *k*, *D*, and *R*

As demonstrated in our previous work[45] and detailed in the Supplementary Information section S4, 3D numerical modeling can be conducted to calculate the temperature rise to determine *k*, *D*, and *R* simultaneously. Take the 2.4-nm-thick $MoS_2$ for example, from the 3D numerical simulation and Raman experiment, we calculate the normalized RSC values as $\Theta_1$, $\Theta_2$ and $\Theta_3$ for

$MoS_2$ in the ($k$, $D$, $R$) space. It should be noted that in our Raman experiment, the measured RSC of $MoS_2$ is Raman-intensity weighted average of the sample. For the zero-transport state, the measured temperature rise is also based on the time average over the pulse width. All of these are also considered in the modeling to evaluate the temperature rise of $MoS_2$. These are detailed in S1 of Supplementary Information.

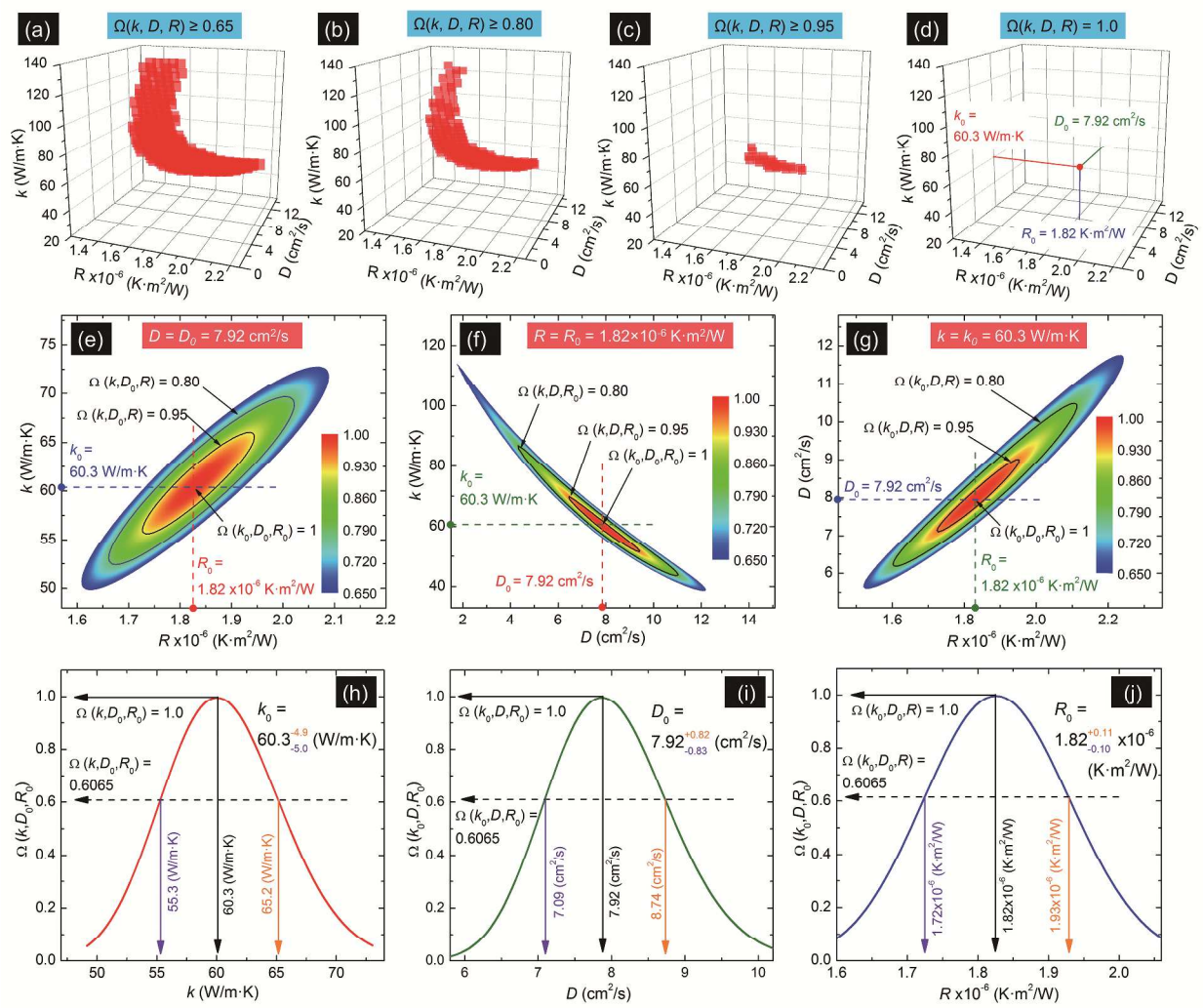


**Figure 4.** Simultaneous determination of $k$, $D$, $R$ of 2.4-nm-thick $MoS_2$ sample. (a)-(d) show the normalized probability distribution function $\Omega(k, D, R)$ with probability of 0.65 in (a), 0.80 in (b), 0.95 in (c), and 1.0 in (d). The point with $\Omega(k, D, R)$ =1.0 gives the simultaneous

determination of *k*, *D*, and *R*. (e)-(g) are the 2D contour of cross-section views of $\Omega(k, D, R)$ =0.65. All those three view planes show the point of $\Omega(k, D, R) = 1$. (h)-(j): the 1D plot from 2D contour to determine the final result uncertainty. (h) gives the 1D plot of $\Omega(k, D, R)$ against thermal conductivity *k* as extracted from (e) or (f). The value of $\Omega = 0.6065$ corresponding to the $\sigma$ probability is used to determine the final result uncertainty. (i) and (j) are for the uncertainties of *D* and *R*.

Then, the normalized probability distribution function ($\Omega$) is used to normalize the (*k*, *D*, *R*) space data to determine the (*k*, *D*, *R*). For each CW heating state, $\Omega_i = \exp\left[-(\Theta_i - \Theta_{\exp\_i})^2 / (2\sigma_i^2)\right]$ (*i* = 1, 2, and 3). $\Theta_i$ and $\Theta_{\exp\_i}$ are normalized RSC value from 3D modeling and experiment, respectively. $\sigma_i$ is the experimental uncertainty. In the (*k*, *D*, *R*) space, a composite probability distribution function is defined as $\Omega(k, D, R) = \Omega_1 \cdot \Omega_2 \cdot \Omega_3$. The position in the (*k*, *D*, *R*) space of $\Omega(k, D, R) = 1.0$ represents the corresponding (*k*, *D*, *R*) results for this sample. For the 2.4-nm-thick sample, as shown in Figure 4 (a), $\Omega(k, D, R) \geq 0.65$ in the (*k*, *D*, *R*) space gives a (*k*, *D*, *R*) range. In this space range, higher than 65% probability is achieved that the final (*k*, *D*, *R*) result is inside. Therefore, if the probability level is increased from 0.65 to 0.80 to 0.95, and to 1.0, as shown in Fig. 4 (b)-(d), the (*k*, *D*, *R*) space range becomes smaller and smaller. As a result, in Fig. 4(d), there is only one point ($k_0$, $D_0$, $R_0$) in the space that could give $\Omega(60.3\,\mathrm{W/m\cdot K}, 7.92\,\mathrm{cm^2/s}, 1.82\times10^{-6}\,\mathrm{K\cdot m^2/W}) = 1.0$. Therefore, *k*, *D*, and *R* are simultaneously determined as $k_0$ = 60.3W/m·K, $D_0$ = 7.92 $\mathrm{cm^2/s}$, and $R_0 = 1.82\times10^{-6}$ $\mathrm{K\cdot m^2/W}$. Figure 4(e)-(g) show the cross-section views of Fig. 4(a) which are the color contours of the different probability levels. All these three cross-section planes go through the point of

$\Omega(k, D, R) = 1$ in the ($k$, $D$, $R$) space. Figure 4(e) presents the 2D $\Omega\ (k, D, R)$ contour in ($k$, $R$) space with $D = D_0 = 7.92$ cm$^2$/s. Two dash lines go through point $\Omega\ (k, D_0, R) = 1.0$ also can be used to determine the $k$ and $R$ value. Also, by extracting the data from dash lines, as shown in Fig 4(h)-(j), a 1D plot of $\Omega\ (k, D, R)$ against $k$, $D$, and $R$, respectively is obtained. The red 1D plot in Fig. 4(h) corresponds to the red dash lines in Fig. 4(e) and (f). Another two 1D plots in Fig. 4(i) and (j) correspond to the green and blue dash lines in Fig. 4(e)-(g), respectively. To show the results with uncertainty, the value of $\Omega\ (k, D, R) = 0.6065$ corresponding to the $\sigma$ probability is used to find the results range. From Fig. 4 (h)-(j), the deduced $k_0$ is determined as $60.3^{+4.9}_{-5.0}$ W/m·K, $D_0$ as $7.92^{+0.82}_{-0.83}$ cm$^2$/s, and $R_0$ as $1.82^{+0.11}_{-0.10} \times 10^{-6}$ K·m$^2$/W. The results and corresponding uncertainty for all eight samples are summarized in Table 1 and also plotted in Fig. 5 (a)-(c). It should be noted that all uncertainties come from the RSC fitting procedure and the uncertainties of $P$, $r_0$, and NA are not included here as they are negligible compared with the uncertainty of the fitting.

**Table 1**. The summary of $k$, $D$, and $R$ of eight $MoS_2$ samples.

| Sample | Number | $k$ (W/m·K) | $D$ (cm$^2$/s) | $R$ ($10^{-6}$ K·m$^2$/W) |
|---|---|---|---|---|
| 2.4 nm | 4 | $60.3^{+4.9}_{-5.0}$ | $7.92^{+0.82}_{-0.83}$ | $1.82^{+0.11}_{-0.10}$ |
| 3.6 nm | 6 | $46.0^{+4.8}_{-4.4}$ | $10.3^{+1.23}_{-1.06}$ | $0.602^{+0.050}_{-0.050}$ |
| 5.0 nm | 8 | $35.1^{+3.7}_{-3.4}$ | $10.2^{+1.32}_{-1.24}$ | $0.798^{+0.065}_{-0.065}$ |
| 9.2 nm | 15 | $31.0^{+3.1}_{-2.9}$ | $8.49^{+1.20}_{-1.07}$ | $0.402^{+0.044}_{-0.044}$ |
| 15.0 nm | 25 | $51.0^{+2.6}_{-2.4}$ | $10.2^{+1.15}_{-1.02}$ | $0.480^{+0.052}_{-0.051}$ |
| 24.6 nm | 41 | $52.4^{+2.8}_{-2.3}$ | $7.63^{+1.20}_{-1.09}$ | $1.07^{+0.13}_{-0.13}$ |
| 30.6 nm | 51 | $62.9^{+2.8}_{-2.5}$ | $6.45^{+1.00}_{-0.92}$ | $0.938^{+0.125}_{-0.124}$ |
| 37.8 nm | 63 | $76.2^{+3.3}_{-2.9}$ | $6.22^{+1.03}_{-0.89}$ | $0.482^{+0.106}_{-0.102}$ |

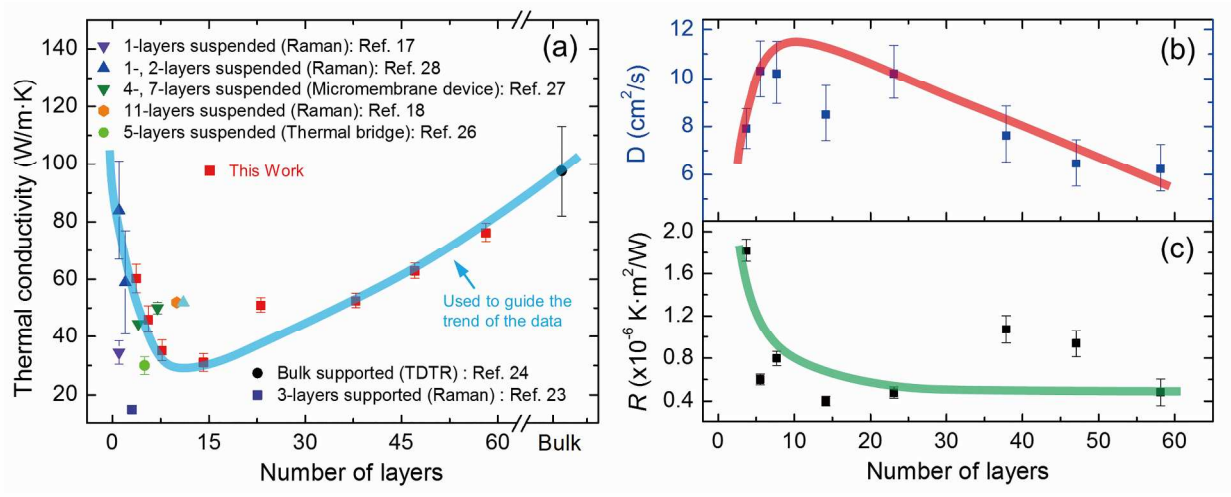


**Figure 5.** (a) Summary of the room temperature in-plane thermal conductivity of $MoS_2$ as a function of layer number for this work (red squares) and other experimentally obtained results. (b)(c) Hot carrier diffusion coefficient ($D$) and interface thermal resistance ($R$) of eight $MoS_2$ samples. The blue, red, and green curves are used to guide the trend of the data visually. Error bars are presented to show the measurement uncertainties.

### 3.3 Thickness-dependent in-plane thermal conductivity of FL $MoS_2$

Fig. 5(a) presents the $k$ of eight 2D FL $MoS_2$ samples at room temperature as a function of the thickness (number of layers). The recent measurement results of other groups are also added for comparison.[12, 17-22] The $k$ value discrepancy from different works could be mainly attributed to the difference in sample structure and measurement methods. In this work, a nonmonotonic thickness-dependent $k$ trend guided by a light blue curve with the nadir at around 6.6-nm-thick (10 layers) is discovered. This agrees well with the results reported to date, especially for the decreasing part (thin $MoS_2$ samples less than ten layers). As studied by first-principles calculations by Gu *et al.*,[47] the thermal conductivity reduction from single-layer to few-layer $MoS_2$ is accounted by the change of phonon dispersion and the enhanced phonon scattering

strength for thicker samples. The changes in the phonon dispersion with increased layer numbers result in a lower group velocity, which could greatly decrease the in-plane *k*. Additionally, similar to graphene, from single-layer to few-layer, the mirror symmetry is missing which changes the anharmonic force constant. This leads to stronger phonon scattering and thermal conductivity reduction.[48] For the positive correlation part of *k* and thickness for 10 to 60-layer $MoS_2$, only bulk $MoS_2$ has been studied to date. 63-layers sample is the thickest sample we measured in this work whose in-plane *k* is still smaller than the measured bulk sample. We believe after 63 layers, the *k* will increase against the thickness slower and finally reach the bulk's value. Our discovered *k*-thickness trend could be explained qualitatively as following. For thick $MoS_2$ flakes, the missing atomic force constant symmetry recovers for the $MoS_2$ layers in the middle. Therefore, only the $MoS_2$ layers next to the surface region have a reduced *k*, while the $MoS_2$ layers in the middle have a *k* close to the bulk value. When the film becomes thicker, this type of surface-layer effect will reduce, leading to a *k* increase toward the bulk value. Besides the atomic force constant effect, for the layers next to the surface, they are more subject to surface phonon scattering effect by surface structure disorder (physical disorder and chemical disorder, e.g. oxidization), which also leads to a *k* decrease. When the film is thicker, this surface defect-phonon scattering effect becomes relatively weaker, which makes the overall in-plane *k* increase. This type of *k* trend has also been demonstrated and explained for regular films and other 2D materials.[49]

### 3.4 Effect of $MoS_2$ thickness on *R* and *D*

Figure 5 (b)-(c) show how *R* and *D* values change with $MoS_2$ thickness. The detailed results are also summarized in Table 1. *D* has a relatively higher uncertainty than both *k* and *R*. As

explained in our previous work,[45] the hot carrier diffusivity is extracted by its effect on thermal energy distribution. Ideally, if extremely small size heating states are generated, the uncertainty of *D* could be largely reduced. Figure 5 (b) presents the nonmonotonic thickness dependent carrier diffusivity *D*. Similar trend has been found in our recent work by referring to the *k* reported by other groups.[41] We attributed this trend to the reduced charge impurities for thin samples, loose contact with the substrate, and possible wet substrate surface for thicker samples. Besides, from Eqs. (1) and (2), the hot carrier diffusivity determined here is dependent on the carrier lifetime. Thus, with this technique, the carrier diffusion length instead of the diffusivity can be firmly determined. An additional discussion for this can be found in Supplementary Information section S5.

The interface thermal resistance *R* for eight samples are in the order of $1.0\times10^{-6}$ $K\cdot m^2/W$. It decreases with increased layer number. We have studied the thickness dependent interface thermal energy transport with a presumed *k*. The thicker sample with better stiffness could help form better contact with the substrate.[30] In addition, the glass substrate used in this work is not polished very well, so the FL $MoS_2$ samples are possibly supported by some high points on the substrate. This is the reason why the *R* is larger than that with the polished silicon substrate.[41]

**3.5 Extended discussion on the ET-Raman capacity and capability**

Using the Five-State ET-Raman technique, the unknown errors in laser absorption evaluation and Raman temperature calibration coefficient could be eliminated. For almost all other optical-thermal technique to study the thermal energy transport, the laser absorption is one of the factors that bring in the most substantial uncertainty.[45, 50] The optical properties which are required to

evaluate the laser absorption rate of the measured material are difficult to determine and always have large sample-to-sample variance. Besides, some temperature-dependent optical properties could also introduce possible errors during the Raman laser heating experiments. In addition, when the Raman temperature calibration experiment is necessary for determining the absolute temperature rise, the thermal expansion coefficient mismatch and temperature measurement in calibration could bring in many unknown errors to the Raman temperature calibration coefficient evaluation.[45, 51] Therefore, large uncertainties of thermal conductivity and interface thermal resistance are expected. Furthermore, the hot carrier diffusion could significantly extend the heating size, especially for the smaller laser heating size scenarios. Simply neglect this diffusion effect on thermal energy transport could result in an overestimated in-plane thermal conductivity and an underestimated interface thermal resistance evaluation.

For future applications, the Five-State ET-Raman can be used to study 2D materials with supported and suspended structures, such as TMDs, black phosphorus, *etc*. However, several points should be noted. For materials with indirect bandgap (e.g., FL $MoS_2$), the energy carried by the hot carriers will be transferred to local phonons because of the restricted radiative carrier recombination. The ET-Raman technique demonstrated in this work could be directly applied to this type of materials. Second, the radiative transitions will dominate the recombination process for materials with direct bandgap (e.g., single-layer $MoS_2$). The physical model needs to be modified by applying a coefficient to the first term of Eq. (2) to describe how much energy could transfer to local phonons. Thirdly, for materials with no bandgap structure (e.g., graphene), the electron will transfer the photon energy to local lattice by electron-phonon scattering. Thus, heat conduction equations for both electron and phonon are needed to cover the diffusion process.

Last, for materials with a hot carrier diffusion length much longer than experimentally achieved largest laser spot size, this technique may not be applicable. This is because the heating area is predominantly determined by the hot carrier diffusion length, and variation of the laser spot size could not differentiate this effect from heat conduction effect. Under such scenario, instead of measuring $k$ and $D$, an effective $k$ can be determined that has the effect of phonon transport and hot carrier diffusion.

For suspended 2D materials, the absorbed laser energy could only dissipate in the in-plane direction. Additionally, there will be a heat accumulation effect. Also, the sample could be easily destroyed because the sample thermal relaxation time is longer. Therefore, to use this technique to characterize suspended 2D materials, the laser should be modulated or a nanosecond-pulsed laser can be used to have a longer cooling time. In particular, the hot carrier effect can be neglected by using laser spot size which is large enough compared with the hot carrier diffusion length. In this case, the physical model could be simplified to determine the in-plane thermal conductivity. At present, work is being conducted in our group by using nanosecond ET-Raman to measure $k$ of suspended 2D materials.

## 4. Conclusion

In this work, we developed a novel Five-State Picosecond ET-Raman for measuring the in-plane thermal conductivity ($k$) of nm-thick 2D materials. It does not require laser absorption and absolute temperature rise evaluation, which increases the measurement accuracy significantly. More importantly, the hot carrier diffusion was taken into full consideration in our $k$ measurement. The in-plane thermal conductivity of eight 2D FL $MoS_2$ samples (thickness

ranging from 2.4 nm to 37.8 nm) supported on glass substrate were successfully measured using this technique. A nonmonotonic thickness-dependent *k* trend was discovered, which is attributed to the possible surface phonon scattering, the change of phonon dispersion and enhanced phonon scattering strength. The measured *k* value spans from 31.0 to 76.2 W/m·K, which is in good agreement with other reported data. Uniquely, our *k* results for tens-layer $MoS_2$ contribute to a full-spectrum thickness-dependent *k* understanding. Aside from the in-plane thermal conductivity, the hot carrier diffusivity *D* and interface thermal resistance *R* were also quantitatively and simultaneously determined. This non-contact measurement uncovers the intrinsic properties of FL $MoS_2$ and provides the first time knowledge of the thickness effect on in-plane *k* of $MoS_2$. The discovery reported in our work will provide new and in-depth knowledge and understanding of how the thickness changes the phonon transport via dispersion and surface structure variation. Also, the new Five-State ps ET-Raman developed in this work will provide one of the most promising techniques for studying the conjugated in-plane and cross-plane phonon transport and hot carrier diffusion in 2D materials.

**Acknowledgments**

Support of this work by National Science Foundation (CBET1235852, CMMI1264399), Department of Energy (DENE0000671), and Iowa Energy Center (OG-17-005) are gratefully acknowledged.

**Conflict of interests**

The authors declare no competing financial interest.

## References


1. K. S. Novoselov, A. K. Geim, S. V. Morozov, D. Jiang, Y. Zhang, S. V. Dubonos, I. V. Grigorieva and A. A. Firsov, *Science*, 2004, **306**, 666-669.
2. S. Z. Butler, S. M. Hollen, L. Cao, Y. Cui, J. A. Gupta, H. R. Gutiérrez, T. F. Heinz, S. S. Hong, J. Huang and A. F. Ismach, *ACS nano*, 2013, **7**, 2898-2926.
3. M. Xu, T. Liang, M. Shi and H. Chen, *Chem. Rev.*, 2013, **113**, 3766-3798.
4. J. Bao, K. Jeppson, M. Edwards, Y. Fu, L. Ye, X. Lu and J. Liu, *Electronic Materials Letters*, 2016, **12**, 1-16.
5. Q. H. Wang, K. Kalantar-Zadeh, A. Kis, J. N. Coleman and M. S. Strano, *Nat. Nanotechnol.*, 2012, **7**, 699-712.
6. K. Kalantar-zadeh, J. Z. Ou, T. Daeneke, A. Mitchell, T. Sasaki and M. S. Fuhrer, *Applied Materials Today*, 2016, **5**, 73-89.
7. A. Kuc, N. Zibouche and T. Heine, *Phys. Rev. B*, 2011, **83**, 245213.
8. B. Radisavljevic, A. Radenovic, J. Brivio, i. V. Giacometti and A. Kis, *Nat. Nanotechnol.*, 2011, **6**, 147-150.
9. K. F. Mak, C. Lee, J. Hone, J. Shan and T. F. Heinz, *Phys. Rev. Lett.*, 2010, **105**, 136805.
10. S. Kim, A. Konar, W.-S. Hwang, J. H. Lee, J. Lee, J. Yang, C. Jung, H. Kim, J.-B. Yoo and J.-Y. Choi, *Nat. Commun.*, 2012, **3**, 1011.
11. K. Kalantar-Zadeh and J. Z. Ou, *ACS Sensors*, 2015, **1**, 5-16.
12. E. Pop, *Nano Res.*, 2010, **3**, 147-169.
13. D. G. Cahill, W. K. Ford, K. E. Goodson, G. D. Mahan, A. Majumdar, H. J. Maris, R. Merlin and S. R. Phillpot, *J. Appl. Phys.*, 2003, **93**, 793-818.
14. M. Buscema, M. Barkelid, V. Zwiller, H. S. van der Zant, G. A. Steele and A. Castellanos-Gomez, *Nano Lett.*, 2013, **13**, 358-363.
15. J. J. Bae, H. Y. Jeong, G. H. Han, J. Kim, H. Kim, M. S. Kim, B. H. Moon, S. C. Lim and Y. H. Lee, *Nanoscale*, 2017, **9**, 2541-2547.
16. Z. Ding, J.-W. Jiang, Q.-X. Pei and Y.-W. Zhang, *Nanotechnol.*, 2015, **26**, 065703.
17. R. Yan, J. R. Simpson, S. Bertolazzi, J. Brivio, M. Watson, X. Wu, A. Kis, T. Luo, A. R. Hight Walker and H. G. Xing, *ACS nano*, 2014, **8**, 986-993.
18. S. Sahoo, A. P. Gaur, M. Ahmadi, M. J.-F. Guinel and R. S. Katiyar, *J. Phys. Chem. C*, 2013, **117**, 9042-9047.
19. J. Liu, G.-M. Choi and D. G. Cahill, *J. Appl. Phys.*, 2014, **116**, 233107.
20. A. Polman and H. A. Atwater, *Nat. Mater.*, 2012, **11**, 174-177.
21. I. Jo, M. T. Pettes, E. Ou, W. Wu and L. Shi, *Appl. Phys. Lett.*, 2014, **104**, 201902.
22. X. Zhang, D. Sun, Y. Li, G.-H. Lee, X. Cui, D. Chenet, Y. You, T. F. Heinz and J. C. Hone, *ACS Appl. Mater. Interfaces*, 2015, **7**, 25923-25929.
23. X. Gu and R. Yang, *Appl. Phys. Lett.*, 2014, **105**, 131903.
24. G. Zhu, J. Liu, Q. Zheng, R. Zhang, D. Li, D. Banerjee and D. G. Cahill, *Nat. Commun.*, 2016, **7**, 13211.
25. M. M. Perera, M.-W. Lin, H.-J. Chuang, B. P. Chamlagain, C. Wang, X. Tan, M. M.-C. Cheng, D. Tománek and Z. Zhou, *Acs Nano*, 2013, **7**, 4449-4458.
26. E. X. Pérez, *Design, fabrication and characterization of porous silicon multilayer optical devices*, Universitat Rovira i Virgili, 2008.
27. H. Wang, K. Kurata, T. Fukunaga, H. Takamatsu, X. Zhang, T. Ikuta, K. Takahashi, T. Nishiyama, H. Ago and Y. Takata, *Sci. Rep.*, 2016, **6**, 21823.

28. S.-M. Lee and D. G. Cahill, *Microscale Thermophys. Eng.*, 1997, **1**, 47-52.
29. J. Zhu, D. Tang, W. Wang, J. Liu, K. W. Holub and R. Yang, *J. Appl. Phys.*, 2010, **108**, 094315.
30. P. Yuan, C. Li, S. Xu, J. Liu and X. Wang, *Acta Mater.*, 2017, **122**, 152-165.
31. T. Wang, R. Wang, P. Yuan, S. Xu, J. Liu and X. Wang, *Adv. Mater. Interfaces*, 2017, **4**, 1700233.
32. A. A. Balandin, S. Ghosh, W. Bao, I. Calizo, D. Teweldebrhan, F. Miao and C. N. Lau, *Nano Lett.*, 2008, **8**, 902-907.
33. T. Beechem, L. Yates and S. Graham, *Rev. Sci. Instrum.*, 2015, **86**, 041101.
34. P. Yuan, J. Liu, R. Wang and X. Wang, *Nanoscale*, 2017, **9**, 6808-6820.
35. X. Wang, *Experimental Micro/nanoscale Thermal Transport*, John Wiley & Sons, 2012.
36. D. Yu, S. Li, W. Qi and M. Wang, *Appl. Phys. Lett.*, 2017, **111**, 123102.
37. G. Plechinger, S. Heydrich, J. Eroms, D. Weissa, C. Schuller and T. Korn, *Appl. Phys. Lett.*, 2012, **101**, 101906-101906-101903.
38. M. Nestoros, B. C. Forget, C. Christofides and A. Seas, *Phys. Rev. B*, 1995, **51**, 14115.
39. C. Christofides, A. Othonos and E. Loizidou, *J. Appl. Phys.*, 2002, **92**, 1280-1285.
40. Z. Nie, R. Long, L. Sun, C.-C. Huang, J. Zhang, Q. Xiong, D. W. Hewak, Z. Shen, O. V. Prezhdo and Z.-H. Loh, *ACS nano*, 2014, **8**, 10931-10940.
41. P. Yuan, T. Hong, W. Ridong, W. Tianyu and W. Xinwei, *RSC Advances*, 2018, **8**, 12767-12778.
42. L. Su, Y. Zhang, Y. Yu and L. Cao, *Nanoscale*, 2014, **6**, 4920-4927.
43. K. G. Zhou, M. Zhao, M. J. Chang, Q. Wang, X. Z. Wu, Y. Song and H. L. Zhang, *Small*, 2015, **11**, 694-701.
44. K. Wang, Y. Feng, C. Chang, J. Zhan, C. Wang, Q. Zhao, J. N. Coleman, L. Zhang, W. J. Blau and J. Wang, *Nanoscale*, 2014, **6**, 10530-10535.
45. P. Yuan, R. Wang, H. Tan, T. Wang and X. Wang, *ACS Photonics*, 2017, **4**, 3115-3129.
46. B. K. Choi, M. Kim, K.-H. Jung, J. Kim, K.-S. Yu and Y. J. Chang, *Nanoscale research letters*, 2017, **12**, 492.
47. A. Pyatenko, M. Yamaguchi and M. Suzuki, *J. Phys. Chem. C*, 2007, **111**, 7910-7917.
48. L. Lindsay, D. Broido and N. Mingo, *Phys. Rev. B*, 2010, **82**, 115427.
49. J. Pu, Y. Yomogida, K.-K. Liu, L.-J. Li, Y. Iwasa and T. Takenobu, *Nano Lett.*, 2012, **12**, 4013-4017.
50. H. Zhang, Y. Ma, Y. Wan, X. Rong, Z. Xie, W. Wang and L. Dai, *Sci. Rep.*, 2015, **5**, 8440.
51. A. Taube, J. Judek, A. Łapińska and M. Zdrojek, *ACS Appl. Mater. Interfaces*, 2015, **7**, 5061-5065.

## Table of Contents Entry

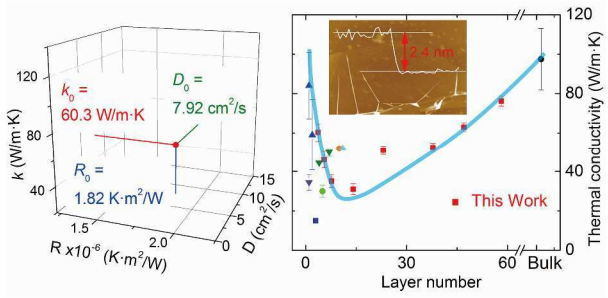


The thermal conductivity of supported $MoS_2$ is discovered to first decrease with thickness (< 9.2 nm), then increase with thickness.